Reduced Dimensionality Quantum Reaction Dynamics of $OH + CH_4 \rightarrow H_2O + CH_3$

Liesbeth M. C. Janssen

January 5, 2008

Supervisors:

Dr. S. T. Banks and Prof. dr. D. C. Clary
Physical and Theoretical Chemistry Laboratory,
University of Oxford, United Kingdom

Dr. ir. G. C. Groenenboom and Prof. dr. ir. A. van der Avoird
Theoretical Chemistry, Institute for Molecules and Materials,
Radboud University Nijmegen, The Netherlands

Summary

A reduced dimensionality quantum dynamics method is described for calculating state-selected reaction cross sections and rate constants for polyatomic reactions. The method treats explicitly the bonds being broken and formed, while the remaining degrees of freedom are accounted for by means of an effective potential. The close-coupled equations are derived in hyperspherical coordinates and solved using the R-matrix propagation scheme. Reaction probabilities are obtained by applying approximate boundary conditions directly in hyperspherical coordinates. The method is applied to the reaction OH + CH_4 $\rightarrow$ H_2O + CH_3. The CH_4OH potential energy surface is obtained by fitting a double Morse analytical function to a set of high level *ab initio* points, with single point energies calculated at the CCSD(T)/cc-pVTZ//MP2/cc-pVTZ level of theory. The zero-point energies of the spectator modes are included prior to fitting to account for the quantum nature of the neglected degrees of freedom. The results indicate that the reaction is significantly enhanced by excitation of the C–H stretch. Calculated differential cross sections show that the H_2O product is predominantly scattered in the backward hemisphere, with a propensity for sideways scattering at high energies. The calculated rate constants compare very favorably with experiment, although the curvature of the Arrhenius plot is not completely reproduced.

Contents

Chapter 1

Introduction

The field of chemical reaction dynamics focuses on the microscopic aspects of chemical reactions, aiming to elucidate the mechanisms that link reactants to products. The development of advanced laser and molecular beam techniques has made it possible to study chemical reactions at a detailed state-to-state level, allowing for accurate measurements of state-resolved cross sections and rate constants. This experimental progress had prompted the emergence of new theoretical methods, both to explain and to predict the outcome of experiments. As a result, chemical reaction dynamics may now be considered as one of the major fields of theoretical chemistry.

The most accurate way to calculate reaction cross sections and rate constants is to use methods based on quantum mechanics. In general, a complete quantum mechanical description of a (polyatomic) reaction involves the explicit treatment of $3N-6$ degrees of freedom, with N denoting the total number of atoms. A full quantum dynamics simulation of such an N atom system requires a $3N-6$ dimensional potential energy surface to enter the Schrödinger equation. In practice, however, the development of multi-dimensional potential energy surfaces can be extremely challenging and time-consuming, which limits the feasibility of a full dimensional approach. Aside from the apparent difficulties in obtaining an accurate potential, the number of dimensions in which quantum scattering calculations can be performed is also restricted. Hence, an exact quantum treatment is only applicable to reactions involving no more than a few atoms [1, 2]. There are now several methods available that seek to address this problem. A widely adopted approach for calculating rate constants is to use methods based on transition state theory (TST) [3]. However, TST is an inherently classical theory and treats quantum effects only in an approximate manner. Conversely, a so-called reduced dimensionality approach maintains an accurate quantum description of the most important degrees of freedom, while the remaining 'spectator' modes are accounted for by approximate methods [4]. Such reduced dimensionality models thus allow for a rigorous quantum treatment of the modes that are most actively involved in the reaction.

In the present work, a two-dimensional quantum scattering model is employed to study the dynamics and kinetics of $OH + CH_4 \rightarrow H_2O + CH_3$. This reaction has received considerable attention in the past due to its importance in combustion and atmospheric chemistry. Experimental studies [5, 6, 7, 8, 9, 10, 11, 12, 13, 14, 15, 16] have shown that the thermal rate constant exhibits non-Arrhenius behaviour, indicating a large degree of tunneling. A correct treatment of quantum effects is thus crucial

for accurately modeling the dynamics and kinetics. The OH + CH_4 system has been studied theoretically using a variety of TST-based methods [17, 18, 19, 20, 21, 22, 23]. The most accurate TST results were obtained by Masgrau *et al.* [23], who employed variational TST with multi-dimensional tunneling corrections at a high level of theory. Their calculated rate constants compared very favorably with experiment, although some discrepancies were found at low temperatures. Furthermore, a small number of reduced dimensionality studies has been reported for the OH + CH_4 → H_2O + CH_3 reaction. Nyman and Clary [24] used the so-called rotating bond approximation, treating explicitly the OH rotation, the stretching vibrations of the reactive bonds, and the bending motion of H_2O. The remaining degrees of freedom were accounted for by an adiabatic approach. Their results indicated that the ground state reaction produces primarily ground state H_2O, while vibrationally excited CH_4 yields excited H_2O products. The rate constants were in reasonably good agreement with experiment, although the low-temperature behaviour of the Arrhenius plot was not fully reproduced. They also calculated the differential cross sections for the ground state reaction [25], and found that the H_2O product is mainly backward and sideways scattered. Yu [26] employed a five-dimensional quantum scattering model to study the dynamics and kinetics of OH + CH_4. The dynamics calculations were performed on an analytical potential energy surface developed by Espinosa-Garcia and Corchado [21]. It was found that vibrational excitations of CH_4 can significantly enhance the reaction, while the influence of the non-reactive O–H bond is negligible. The calculated rate constants captured the curvature of the Arrhenius plot very accurately, but slightly underestimated the rate at high temperatures.

In this work, a two-dimensional quantum scattering method is described that treats explicitly the bonds being broken and formed [27]. The contributions from the spectator modes are accounted for by means of an effective *ab initio* potential. A significant advantage of this method is that the dynamics simulations can be performed without constructing a full dimensional potential energy surface. The method is developed specifically for collinear polyatomic reactions and is applicable to a wide range of systems [27, 28, 29]. The present study describes both the general theory and the application to OH + CH_4 → H_2O + CH_3.

Chapter 2

Theory

This chapter gives a general description of the reduced dimensionality model used in the scattering calculations. The model applies to any reaction with a collinear reaction path. The coordinate system is defined in section 2.1 and the Hamiltonian is discussed in section 2.2. The solutions to the Schrödinger equation are derived in sections 2.3 and 2.4, starting with the close-coupled equations and followed by the derivation of the scattering matrix. Finally, the reaction cross sections and rate constants are given in section 2.5.

2.1 Coordinate system

For a collinear atom-diatom reaction A + BC → AB + C, the Jacobi coordinates of the reactants are the distance R_{A} between A and the center of mass of BC and the distance r_{BC} between B and C. These coordinates correspond to the relative translational motion of A towards BC and the vibrational motion of BC, respectively. The Jacobi coordinates describing the products are the distance R_{C} between C and the center of mass of AB and the distance r_{AB} between A and B [30]. Both sets of coordinates are shown in Figure 2.1.

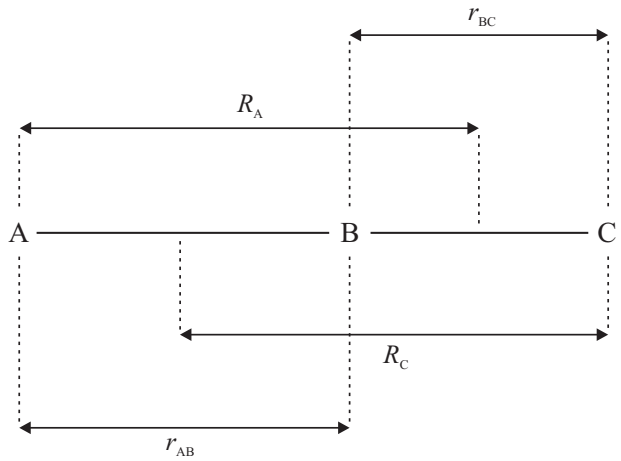

Figure 2.1: Jacobi coordinates for a collinear triatomic reaction A + BC → AB + C.

In order to simplify the scattering problem, the Jacobi coordinates may be scaled

by a mass-dependent factor [30, 31]:

$$R_\alpha = \left(\frac{M_{\alpha 1}}{\mu}\right)^{1/2} R_{\mathrm{A}}, \tag{2.1}$$

$$r_\alpha = \left(\frac{M_{\alpha 2}}{\mu}\right)^{1/2} r_{\mathrm{BC}}, \tag{2.2}$$

$$R_\gamma = \left(\frac{M_{\gamma 1}}{\mu}\right)^{1/2} R_{\mathrm{C}}, \tag{2.3}$$

$$r_\gamma = \left(\frac{M_{\gamma 2}}{\mu}\right)^{1/2} r_{\mathrm{AB}}. \tag{2.4}$$

The scaling factors are given by:

$$M_{\alpha 1} = \frac{m_{\mathrm{A}}\,(m_{\mathrm{B}} + m_{\mathrm{C}})}{m_{\mathrm{A}} + m_{\mathrm{B}} + m_{\mathrm{C}}}, \tag{2.5}$$

$$M_{\alpha 2} = \frac{m_{\mathrm{B}} m_{\mathrm{C}}}{m_{\mathrm{B}} + m_{\mathrm{C}}}, \tag{2.6}$$

$$M_{\gamma 1} = \frac{m_{\mathrm{C}}\,(m_{\mathrm{A}} + m_{\mathrm{B}})}{m_{\mathrm{A}} + m_{\mathrm{B}} + m_{\mathrm{C}}}, \tag{2.7}$$

$$M_{\gamma 2} = \frac{m_{\mathrm{A}} m_{\mathrm{B}}}{m_{\mathrm{A}} + m_{\mathrm{B}}}, \tag{2.8}$$

where m_{A}, m_{B}, and m_{C} denote the atomic masses. The reduced mass μ is defined as:

$$\mu = \left(\frac{m_{\mathrm{A}} m_{\mathrm{B}} m_{\mathrm{C}}}{m_{\mathrm{A}} + m_{\mathrm{B}} + m_{\mathrm{C}}}\right)^{1/2}. \tag{2.9}$$

The use of mass-scaled Jacobi coordinates simplifies the problem in such a way that each type of motion occurs with the same mass μ. This holds for both arrangement channels. The mass-scaled Jacobi coordinates of the reactants and products are related to each other by the following transformation [30]:

$$\begin{pmatrix} R_\gamma \\ r_\gamma \end{pmatrix} = \begin{pmatrix} \cos\theta & \sin\theta \\ \sin\theta & -\cos\theta \end{pmatrix} \begin{pmatrix} R_\alpha \\ r_\alpha \end{pmatrix}, \tag{2.10}$$

where θ is the skewing angle between the two arrangements (see Figure 2.2):

$$\tan\theta = \left[\frac{m_{\mathrm{B}}\,(m_{\mathrm{A}} + m_{\mathrm{B}} + m_{\mathrm{C}})}{m_{\mathrm{A}} m_{\mathrm{C}}}\right]^{1/2}. \tag{2.11}$$

Although mass-scaled Jacobi coordinates are suitable for describing the asymptotic reactant and product channels, they only apply to a limited region of coordinate space. The coordinate system (R_α, r_α) is only relevant for the reactant arrangement, while (R_γ, r_γ) uniquely describes the products. Since all molecular arrangements must be treated simultaneously in the scattering calculations, the coordinate systems (R_α, r_α) and (R_γ, r_γ) need to be matched in the interaction region [30]. In order to overcome this difficulty, the mass-scaled Jacobi coordinates may be transformed into hyperspherical (polar) coordinates, which have the advantage of moving smoothly from reactants

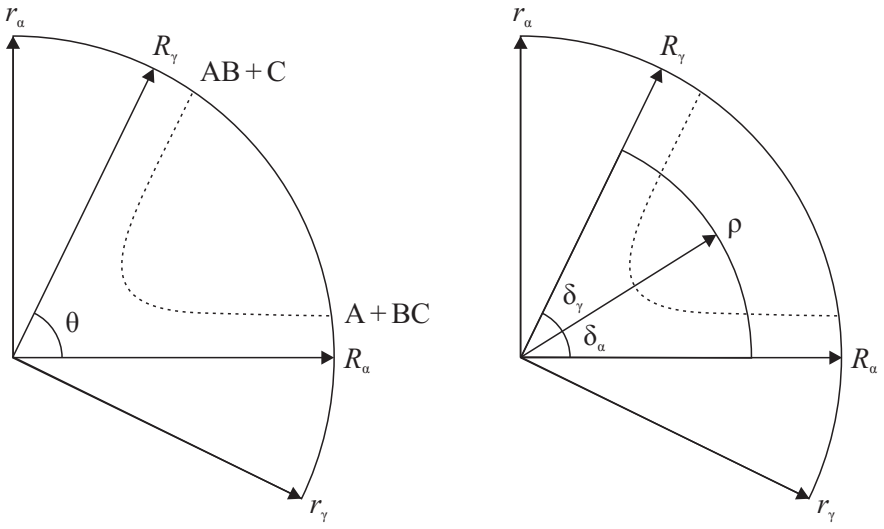

Figure 2.2: Mass-scaled Jacobi coordinates (left) and hyperspherical coordinates (right) for the reaction A + BC → AB + C. The dashed line indicates a typical reaction path for a collinear reaction.

to products [30]. The hyperspherical radius ρ is independent of the arrangement label i, and is given by:

$$\rho = \left(R_i^2 + r_i^2\right)^{1/2}. \tag{2.12}$$

The hyperspherical angle δ_i is defined as:

$$\delta_i = \arctan\left(\frac{r_i}{R_i}\right), \tag{2.13}$$

where $i = \alpha$ corresponds to the reactant channel and $i = \gamma$ to the product channel (see Figure 2.2). It can be shown from Eq. (2.10) that δ_α and δ_γ must sum to the skewing angle θ [30]:

$$\delta_\alpha + \delta_\gamma = \theta. \tag{2.14}$$

As a consequence, δ_α and δ_γ may be replaced by a single coordinate δ that ranges from 0 to $\delta_{max} = \theta$. This readily implies that only one set of Jacobi coordinates (R_i, r_i) is needed to define the hyperspherical coordinate system (ρ, δ).

In principle, the two-dimensional coordinate system described above is only relevant for collinear atom-diatom reactions. However, a similar set of coordinates may be defined for polyatomic reactions using a pseudo-triatomic approach [27]. For a collinear pseudo-triatomic reaction of the type A + B(CD) → AB + (CD), the Jacobi coordinates of the product arrangement are the distance $R_{(\mathrm{CD})}$ between the centers of mass of AB and CD and the distance r_{AB} between A and B. The corresponding mass-scaled Jacobi coordinates are given by [27]:

$$R_\gamma = \left(\frac{M_{\gamma 1}}{\mu}\right)^{1/2} R_{(\mathrm{CD})}, \tag{2.15}$$

$$r_\gamma = \left(\frac{M_{\gamma 2}}{\mu}\right)^{1/2} r_{\mathrm{AB}}, \tag{2.16}$$

where

$$M_{\gamma 1} = \frac{(m_{\rm A} + m_{\rm B})\,(m_{\rm C} + m_{\rm D})}{m_{\rm A} + m_{\rm B} + m_{\rm C} + m_{\rm D}}, \tag{2.17}$$

$$M_{\gamma 2} = \frac{m_{\rm A} m_{\rm B}}{m_{\rm A} + m_{\rm B}}, \tag{2.18}$$

and μ is the reduced mass of the system:

$$\mu = \left(\frac{m_{\rm A} m_{\rm B} m_{\rm C} m_{\rm D}}{m_{\rm A} + m_{\rm B} + m_{\rm C} + m_{\rm D}} \right)^{1/3}. \tag{2.19}$$

The hyperspherical radius ρ then follows directly from Eq. (2.12). The maximum value of δ is defined by the skewing angle θ:

$$\tan\theta = \left[\frac{m_{\rm B}\,(m_{\rm A} + m_{\rm B} + m_{\rm C} + m_{\rm D})}{m_{\rm A}\,(m_{\rm C} + m_{\rm D})} \right]^{1/2}. \tag{2.20}$$

The two-dimensional coordinate system for a collinear pseudo-triatomic reaction (A'A) + B(CD) → (A'A)B + (CD) can be derived in a similar way. The Jacobi coordinates of the products are the distance $R_{\rm (CD)}$ between the centers of mass of A'AB and CD and the distance $r_{\rm AB}$ between the center of mass of A'A and B. The mass-scaled Jacobi coordinates are equivalent to those given in Eqs. (2.15) – (2.19), with the exception that $m_{\rm A}$ is replaced by $(m_{\rm A'} + m_{\rm A})$. The hyperspherical coordinates can be obtained using Eqs. (2.12) and (2.20), where again $m_{\rm A}$ must be substituted by $(m_{\rm A'} + m_{\rm A})$.

2.2 Hamiltonian and potential energy surface

The Hamiltonian used in this study is based on the Bending-Corrected Rotating Linear Model (BCRLM), a reduced dimensionality method developed by Walker and Hayes [31] to treat collinear reactions of the type A + BC → AB + C. In this approach, the bonds being broken and formed are treated explicitly in the scattering calculations, while the remaining spectator (bending) mode is accounted for by means of an effective potential. The Hamiltonian in hyperspherical coordinates is given by [27, 31]:

$$\hat{H} = -\frac{\hbar^2}{2\mu} \left[\frac{\partial^2}{\partial\rho^2} + \frac{1}{\rho^2} \frac{\partial^2}{\partial\delta^2} - \frac{3}{4\rho^2} \right] + \frac{\hat{J}^2}{2\mu\rho^2} + V(\rho, \delta), \tag{2.21}$$

where $\hat{J}^2$ is the total angular momentum operator and $\mathrm{V}(\rho, \delta)$ is the effective potential energy surface. The spectator mode is implicitly taken into account by adding the bending zero-point energy (ZPE) to the collinear interaction potential, i.e. the bending energy is absorbed in $\mathrm{V}(\rho, \delta)$. This method is analogous to the Collinear Exact Quantum Bending-corrected (CEQB) method of Bowman *et al.* [32]. The CEQB model has been extended to polyatomic systems by including all ZPEs of the spectator modes in the effective potential [33, 34]. The present work is based on a similar approach, and is essentially an extension of the BCRLM method to treat collinear polyatomic reactions.

The ZPEs of the spectator modes can be obtained by diagonalizing the so-called mass-weighted Hessian matrix **H**. This matrix contains the second partial derivatives

of the interaction potential with respect to the mass-weighted Cartesian coordinates, i.e. the Cartesian coordinates weighted by the square root of the atomic masses. The eigenvectors $\mathbf{q}_i$ of the mass-weighted Hessian are the normal modes of the system, and the corresponding eigenvalues ϵ_i are related to the frequencies ν_i as [35, 36]:

$$\nu_i = \frac{1}{2\pi}\sqrt{\epsilon_i}. \tag{2.22}$$

In general, the frequencies of the translational and rotational modes should be exactly zero. Due to convergence difficulties, however, these values may be as large as ~ 50 cm^{-1}, which could give rise to mode mixing [35]. To ensure that all vibrational normal modes correspond to pure vibrational motions, the translational and rotational modes are usually separated out before diagonalizing the Hessian [35, 36]. A similar method can be applied to the bonds that are treated explicitly in the scattering calculations. These bonds are constrained at each point of the potential, and their vibrational motions may be mixed into several different modes. By projecting the constraints out of the Hessian (prior to diagonalization), the contributions from the reactive bonds are essentially removed from $\mathbf{H}$. This ensures that the spectator modes are fully decoupled from the reactive modes.

The constraints can be removed using the projection operator formalism described by Lu and Truhlar [37]. The Hessian that needs to be diagonalized, $\mathbf{H}^P$, is given by:

$$\mathbf{H}^P = (\mathbf{1} - \mathbf{P})\mathbf{H}(\mathbf{1} - \mathbf{P}), \tag{2.23}$$

where $\mathbf{1}$ is a $3N \times 3N$ unit matrix (N denotes the total number of atoms) and $\mathbf{P}$ is the projection operator. In the present case, the constraints that are projected out correspond to the motions along A–B and B–C. The projection operator then becomes:

$$\mathbf{P} = \mathbf{e}_{\mathrm{AB}}\mathbf{e}_{\mathrm{AB}}^{\dagger} + \mathbf{e}_{\mathrm{BC}}\mathbf{e}_{\mathrm{BC}}^{\dagger}, \tag{2.24}$$

where $\mathbf{e}_{\mathrm{AB}}$ and $\mathbf{e}_{\mathrm{BC}}$ are $3N$-dimensional orthogonal unit vectors and $\dagger$ denotes the transpose. These orthogonal vectors can be obtained by orthogonalizing the unit vectors $\mathbf{e}^0_{\mathrm{AB}}$ and $\mathbf{e}^0_{\mathrm{BC}}$, which have the general form:

$$\mathbf{e}^0_{\alpha\beta} = \begin{pmatrix} 0 \\ \vdots \\ R_{\alpha x} \\ R_{\alpha y} \\ R_{\alpha z} \\ \vdots \\ R_{\beta x} \\ R_{\beta y} \\ R_{\beta z} \\ \vdots \\ 0 \end{pmatrix}. \tag{2.25}$$

The six nonzero elements of $\mathbf{e}^0_{\alpha\beta}$ are given by:

$$R_{\alpha i} = \frac{N_{\alpha\beta}}{d_{\alpha\beta}}\left[(m_\beta/m_\alpha)^{1/2}x_{\alpha i} - x_{\beta i}\right], \tag{2.26}$$

$$R_{\beta i} = \frac{N_{\alpha\beta}}{d_{\alpha\beta}}\left[(m_\alpha/m_\beta)^{1/2}x_{\beta i} - x_{\alpha i}\right], \tag{2.27}$$

where $N_{\alpha\beta}$ is a normalization constant, $d_{\alpha\beta}$ is the distance between atoms α and β, and $x_{\alpha i}$ and $x_{\beta i}$ are the mass-weighted Cartesian coordinates of the atoms ($i = x, y, z$). Note that the definition of $N_{\alpha\beta}$ given by Lu and Truhlar [37] is only valid for $d_{\alpha\beta} = 1$, and hence this expression should be treated with caution. The vectors $\mathbf{e}^0_{\mathrm{AB}}$ and $\mathbf{e}^0_{\mathrm{BC}}$ can be orthogonalized using a standard Gram-Schmidt procedure, yielding the unit vectors $\mathbf{e}_{\mathrm{AB}}$ and $\mathbf{e}_{\mathrm{BC}}$. Substituting these into Eq. (2.24) gives the appropriate projection operator and $\mathbf{H}^P$ then follows from Eq. (2.23). After diagonalizing this matrix, the eigenvalues of the translational, rotational, and reactive modes should be equal to zero. The remaining $3N-8$ nonzero eigenvalues of $\mathbf{H}^P$, i.e. the eigenvalues of the spectator modes, are then used to calculate the ZPE corrections for $V(\rho, \delta)$. The ZPEs are given by:

$$E_i = \frac{1}{2} h\nu_i, \tag{2.28}$$

where E_i is the zero-point energy and ν_i is the frequency of mode i. Adding these $(3N-8)$ energy terms to the collinear interaction potential finally gives the effective potential energy surface of Eq. (2.21).

2.3 Close-coupled equations

The wave functions of the (pseudo)-triatomic system can be found by solving the Schrödinger equation:

$$\hat{H}\psi = E\psi, \tag{2.29}$$

where $\hat{H}$ is the Hamiltonian given in Eq. (2.21) and E is the total energy. The first step in solving Eq. (2.29) is to divide the coordinate space into small concentric sectors of (nearly) constant ρ. Within each sector i, the terms $1/\rho^2$ and $V(\rho, \delta)$ can be approximated as:

$$1/\rho^2 \simeq 1/\rho_i^2, \tag{2.30}$$

$$V(\rho, \delta) \simeq V(\delta; \rho_i), \tag{2.31}$$

where ρ_i is the value of ρ in the center of the i-th sector. The Hamiltonian in sector i is then given by:

$$\hat{H}^{(i)} \simeq -\frac{\hbar^2}{2\mu}\left[\frac{\partial^2}{\partial\rho^2} - \frac{3}{4\rho_i^2}\right] + \frac{\hat{J}^2}{2\mu\rho_i^2} + \hat{H}_\delta^{(i)}, \tag{2.32}$$

where

$$\hat{H}_\delta^{(i)} = -\frac{\hbar^2}{2\mu\rho_i^2}\frac{\partial^2}{\partial\delta^2} + V(\delta; \rho_i). \tag{2.33}$$

Diagonalizing the δ-dependent part of the Hamiltonian yields the so-called hyperspherical adiabats $\epsilon_{k'}(\rho_i)$ and the corresponding eigenfunctions $\phi_{k'}(\delta; \rho_i)$:

$$\hat{H}_\delta^{(i)}\phi_{k'}(\delta; \rho_i) = \epsilon_{k'}(\rho_i)\phi_{k'}(\delta; \rho_i), \tag{2.34}$$

$$\int \phi_{k'}(\delta; \rho_i)\phi_{k''}(\delta; \rho_i)d\delta = \delta_{k'k''}, \tag{2.35}$$

where $\delta_{k'k''}$ denotes a Kronecker delta. In the asymptotic region (large ρ), the wave functions $\phi_{k'}(\delta; \rho_i)$ become localized eigenstates of either the reactant or product arrangement. The expectation value of δ can be used to identify these asymptotic

channels [27]:

$$\langle \delta \rangle = \langle \phi_{k'}(\delta;\rho_i) \mid \delta \mid \phi_{k'}(\delta;\rho_i) \rangle. \tag{2.36}$$

The eigenfunctions of $\hat{H}^{(i)}$ can now be written as:

$$\psi_k(\rho,\delta;\rho_i) = \sum_{k'}^{K} \phi_{k'}(\delta;\rho_i) f_{k'k}(\rho;\rho_i), \tag{2.37}$$

where K is the size of the contracted basis. This value should be chosen large enough to include all open (energetically accessible) channels. By substituting Eqs. (2.32) and (2.37) into Eq. (2.29) and dividing by $-\hbar^2/2\mu$, the Schrödinger equation may be rewritten as:

$$\sum_{k'}^{K} \left[\frac{\partial^2}{\partial\rho^2} - \frac{3}{4\rho_i^2} - \frac{J(J+1)}{\rho_i^2} - \frac{2\mu\epsilon_{k'}(\rho_i)}{\hbar^2} + \frac{2\mu E}{\hbar^2} \right] \phi_{k'}(\delta;\rho_i) f_{k'k}(\rho;\rho_i) = 0. \tag{2.38}$$

Note that the total angular momentum operator $\hat{J}^2$ has been replaced by its eigenvalues $J(J+1)\hbar^2$. The coordinates on which $\hat{J}^2$ acts are, however, not explicitly taken into account. Pre-multiplying Eq. (2.38) by $\phi_j(\delta;\rho_i)$ and integrating over δ yields:

$$\frac{d^2}{d\rho^2} f_{jk}(\rho;\rho_i) + \left[\frac{2\mu E}{\hbar^2} - \frac{3}{4\rho_i^2} - \frac{J(J+1)}{\rho_i^2} - \frac{2\mu\epsilon_j(\rho_i)}{\hbar^2} \right] f_{jk}(\rho;\rho_i) = 0, \tag{2.39}$$

which in matrix form becomes:

$$\frac{d^2}{d\rho^2}\boldsymbol{f}(\rho;\rho_i) + \mathbf{W}(\rho_i)\boldsymbol{f}(\rho;\rho_i) = 0. \tag{2.40}$$

The matrix elements of $\mathbf{W}$ are given by:

$$W_{jk}(\rho_i) = \frac{2\mu}{\hbar^2} \left[E - \frac{3\hbar^2}{8\mu\rho_i^2} - \frac{J(J+1)\hbar^2}{2\mu\rho_i^2} - \epsilon_j(\rho_i) \right] \delta_{jk}. \tag{2.41}$$

The second order differential equations of Eqs. (2.39) and (2.40) are collectively known as the close-coupled equations. The remaining task is to solve these equations in each sector i, and to match the solutions $f_{jk}(\rho;\rho_i)$ (and their derivatives) at the sector boundaries. This can be done using the R-matrix propagation method.

2.4 R-matrix propagation and scattering matrix

The R-matrix propagation method, as described by Stechel *et al.* [38], is a recursive method for solving linear differential equations of the form

$$\frac{d^2}{d\rho^2}\boldsymbol{f}(\rho) + \mathbf{W}(\rho)\boldsymbol{f}(\rho) = 0. \tag{2.42}$$

The basic idea is to propagate the wave functions from a sector near the origin (small ρ) towards the asymptotic region by means of a global R-matrix. This matrix relates the wave functions to their normal derivatives at the outer (right hand) boundary of

each sector. Within a given sector i, the wave functions at the boundaries can be written as:

$$\boldsymbol{f}_L(\rho_i) = \boldsymbol{f}(\rho_i - \tfrac{1}{2}h_i), \tag{2.43}$$
$$\boldsymbol{f}_R(\rho_i) = \boldsymbol{f}(\rho_i + \tfrac{1}{2}h_i), \tag{2.44}$$

where h_i is the width of the sector. The global R-matrix in sector i is defined as:

$$\boldsymbol{f}_R(\rho_i) = \mathbf{R}(i)\boldsymbol{f}'_R(\rho_i), \tag{2.45}$$

where the prime denotes differentiation with respect to ρ. Enforcing the requirement that $\boldsymbol{f}(\rho)$ and $\boldsymbol{f}'(\rho)$ must be continuous in ρ leads to the following equations:

$$\boldsymbol{f}_L(\rho_{i+1}) = \mathbf{Q}^\dagger(i,i+1)\boldsymbol{f}_R(\rho_i), \tag{2.46}$$
$$\boldsymbol{f}'_L(\rho_{i+1}) = \mathbf{Q}^\dagger(i,i+1)\boldsymbol{f}'_R(\rho_i), \tag{2.47}$$

where $\mathbf{Q}(i,i+1)$ is the transformation matrix that takes the diagonal basis in sector i to that in sector $i+1$:

$$Q_{jk}(i,i+1) = \langle \phi_j(\delta;\rho_i) \mid \phi_k(\delta;\rho_{i+1}) \rangle. \tag{2.48}$$

The global R-matrix $\mathbf{R}(i)$ can be propagated to sector $i+1$ by constructing a local R-matrix $\mathbf{r}(i+1)$. This matrix is defined as:

$$\begin{bmatrix} \boldsymbol{f}_L(\rho_{i+1}) \\ \boldsymbol{f}_R(\rho_{i+1}) \end{bmatrix} = \begin{bmatrix} \mathbf{r}^{(1)}(i+1) & \mathbf{r}^{(2)}(i+1) \\ \mathbf{r}^{(2)}(i+1) & \mathbf{r}^{(1)}(i+1) \end{bmatrix} \begin{bmatrix} -\boldsymbol{f}'_L(\rho_{i+1}) \\ \boldsymbol{f}'_R(\rho_{i+1}) \end{bmatrix}. \tag{2.49}$$

The elements of $\mathbf{r}(i+1)$ are given by:

$$r^{(1)}_{jk}(i+1) = \delta_{jk} \begin{cases} |\lambda_k|^{-1} \coth|h_{i+1}\lambda_k|, & \lambda^2 < 0 \\ -|\lambda_k|^{-1} \cot|h_{i+1}\lambda_k|, & \lambda^2 \geq 0 \end{cases} \tag{2.50}$$

$$r^{(2)}_{jk}(i+1) = \delta_{jk} \begin{cases} |\lambda_k|^{-1} \operatorname{csch}|h_{i+1}\lambda_k|, & \lambda^2 < 0 \\ -|\lambda_k|^{-1} \csc|h_{i+1}\lambda_k|, & \lambda^2 \geq 0 \end{cases} \tag{2.51}$$

where λ_k is the square root of the diagonal matrix element $W_{kk}(\rho_{i+1})$. The values of λ^2 correspond to the total translational energy of the system. Channels with $\lambda^2 < 0$ thus have negative kinetic energy and are locally closed. Open channels correspond to positive kinetic energy ($\lambda^2 \geq 0$). Once the local R-matrix $\mathbf{r}(i+1)$ is known, the global R-matrix $\mathbf{R}(i+1)$ can be obtained using the following recursion relations:

$$\mathbf{R}(i+1) = \mathbf{r}^{(1)}(i+1) - \mathbf{r}^{(2)}(i+1)\mathbf{Z}(i+1)\mathbf{r}^{(2)}(i+1), \tag{2.52}$$
$$\mathbf{Z}(i+1) = \left[\mathbf{r}^{(1)}(i+1) + \mathbf{Q}^\dagger(i,i+1)\mathbf{R}(i)\mathbf{Q}(i,i+1)\right]^{-1}. \tag{2.53}$$

The propagation is initiated near the origin, where the wave functions must satisfy:

$$\boldsymbol{f}(\rho) \xrightarrow{\rho\to 0} 0. \tag{2.54}$$

In that case, the initial R-matrix is given by:

$$R_{jk}(1) = \delta_{jk}|\lambda_k|^{-1}. \tag{2.55}$$

The recursion relations of Eqs. (2.52) and (2.53) can then be used repeatedly until the boundary of the global R-matrix lies in the asymptotic region. The corresponding wave functions form the solutions to Eq. (2.42).

Once the close-coupled equations have been solved, the so-called scattering S-matrix ($\mathbf{S}$) can be extracted. The S-matrix elements $S^J_{jk}(E)$ give the probability amplitude for a transition from initial state j to final state k as a function of E and J. If the S-matrix is known for sufficiently many reactant and product channels, all possible observables of the scattering process, e.g. state-to-state reaction cross sections and rate constants, may be readily determined. Hence, the scattering matrix is one of the most important quantities in theoretical reaction dynamics [30]. The S-matrix can be obtained by enforcing asymptotic boundary conditions at the end of the propagation. In principle, these boundary conditions must be expressed in (mass-scaled) Jacobi coordinates [31, 39]. A much simpler approach, however, is to apply approximate boundary conditions in hyperspherical coordinates [39]:

$$\boldsymbol{f}(\rho) \quad \xrightarrow{\rho\to\infty} \quad \mathbf{I}(\rho) - \mathbf{O}(\rho)\mathbf{S}. \tag{2.56}$$

The incoming ($\mathbf{I}$) and outgoing ($\mathbf{O}$) asymptotic wave functions are defined as:

$$I_{jk}(\rho_n) = \lambda_k^{-1/2} \exp(-i\lambda_k\rho_n)\delta_{jk}, \tag{2.57}$$

$$O_{jk}(\rho_n) = \lambda_k^{-1/2} \exp(i\lambda_k\rho_n)\delta_{jk}, \tag{2.58}$$

where n labels the final sector of ρ. Combining Eqs. (2.56) – (2.58) with the R-matrix of Eq. (2.45) then gives:

$$\mathbf{I}(\rho_n) - \mathbf{O}(\rho_n)\mathbf{S} = \mathbf{R}(n)\left[\mathbf{I}'(\rho_n) - \mathbf{O}'(\rho_n)\mathbf{S}\right], \tag{2.59}$$

which leads directly to the expression for the scattering matrix:

$$\mathbf{S} = \left[\mathbf{R}(n)\mathbf{O}'(\rho_n) - \mathbf{O}(\rho_n)\right]^{-1}\left[\mathbf{R}(n)\mathbf{I}'(\rho_n) - \mathbf{I}(\rho_n)\right]. \tag{2.60}$$

This matrix contains the probability amplitudes for all possible transitions, i.e. for elastic, inelastic, and reactive scattering processes. The S-matrix elements $S^J_{jk}(E)$ are related to the state-to-state probabilities $P^J_{jk}(E)$ as:

$$P^J_{jk}(E) = |S^J_{jk}(E)|^2. \tag{2.61}$$

In general, these state-to-state probabilities should converge as $\rho_n \to \infty$. However, due to the non-exact separability of motion in ρ and δ, the values of $P^J_{jk}(E)$ may oscillate as a function of ρ_n. This problem can be circumvented by averaging the state-to-state probabilities over a number of sectors in the asymptotic region [29, 39].

2.5 Cross sections and rate constants

Once the scattering matrix and state-to-state probabilities are known, the reaction cross sections and rate constants can be calculated. The initial state-selected integral reaction cross-sections are defined as:

$$\sigma_s(E) = \frac{\pi}{q_s^2}\sum_{s'}\sum_{J=0}^{J_{max}}(2J+1)P^J_{ss'}(E), \tag{2.62}$$

where s and s' denote the quantum numbers of the (initial) reactant and (final) product states, respectively. These quantum numbers correspond to the stretching vibrations of the A–B and B–C bonds. The factor q_s^2 in Eq. (2.62) represents the initial translational wave number:

$$q_s^2 = \frac{2\mu_R}{\hbar^2}(E - \epsilon_s), \tag{2.63}$$

where μ_R is the reduced mass of the reactants and ϵ_s is the eigenenergy of $\phi_s(\delta; \rho_i)$ as $\rho_i \to \infty$. The value of J_{max} should be chosen large enough to ensure convergence of the cross sections. The state-to-state differential cross sections are given by:

$$\sigma_{ss'}(\theta) = \frac{1}{4q_s^2}\left|\sum_J^{J_{max}} (2J+1) S_{ss'}^J P_J(\cos\theta)\right|^2, \tag{2.64}$$

where θ denotes the scattering angle and $P_J(\cos\theta)$ is the Jth order Legendre polynomial. The scattering angle is defined such that $\theta = 0$ corresponds to forward scattering and $\theta = \pi$ to backward scattering. Note that the differential cross sections are expressed in terms of the S-matrix elements $S_{ss'}^J(E)$ rather than the (averaged) state-to-state reaction probabilities. Since the elements of the S-matrix are generally complex, the method of averaging over a number of sectors in the asymptotic region cannot be applied here. Hence, the values of $S_{ss'}^J(E)$ and $\sigma_{ss'}(\theta)$ should be treated with some caution. An alternative approach would be to evaluate the differential cross sections in a range of sectors, and average these instead of the S-matrix elements. However, it has been shown that this approximation does not significantly change the qualitative result [29].

The exact thermal rate constant is defined as [40]:

$$k(T) = \frac{1}{hQ_r(T)} \int_0^\infty N(E) e^{-E/k_B T} dE, \tag{2.65}$$

where $Q_r(T)$ is the total partition function for the reactants and $N(E)$ is the cumulative reaction probability (CRP). The exact CRP can be obtained by summing the state-to-state reaction probabilities over all initial and final states, including those of the spectator modes. Since the excited states of the spectator modes are not included in $P_{ss'}^J(E)$, the calculated reaction probabilities must be corrected for these contributions. This can be done using the following energy shift approximation [24, 41]:

$$P_{ss',\mathbf{n}}^J(E) \simeq P_{ss'}^J(E - E_{\mathbf{n}}^\ddagger), \tag{2.66}$$

where $\mathbf{n}$ collectively labels the quantum states of the excited spectator modes and $E_{\mathbf{n}}^\ddagger$ is the energy difference between the excited and ground state spectator modes at the transition state. A similar approximation can be made for the J-dependence of $P_{ss'}(E)$. Instead of evaluating $P_{ss'}^J(E)$ explicitly for each value of J, the state-to-state reaction probabilities for $J > 0$ may be approximated as [41]:

$$P_{ss'}^J(E) \simeq P_{ss'}^{J=0}(E - E_J^\ddagger), \tag{2.67}$$

where $E_J^\ddagger$ is the rotational energy of the transition state. Equation (2.67) readily implies that the close-coupled equations need to be solved only for $J = 0$ in order to

calculate the CRP. Applying both approximations leads to the following expressions for the state-to-state and thermal rate constants [24, 27]:

$$k_{ss'}(T) = \frac{Q^{\ddagger}(T)}{hQ_r(T)} \int_0^{\infty} P_{ss'}^{J=0}(E) e^{-E/k_B T} dE, \tag{2.68}$$

$$k(T) = \frac{Q^{\ddagger}(T)}{hQ_r(T)} \int_0^{\infty} N^{J=0}(E) e^{-E/k_B T} dE, \tag{2.69}$$

where $Q^{\ddagger}(T)$ is the partition function at the transition state for all modes not explicitly treated in the scattering calculations and $N^{J=0}(E)$ is the cumulative reaction probability for $J = 0$:

$$N^{J=0}(E) = \sum_s \sum_{s'} P_{ss'}^{J=0}(E). \tag{2.70}$$

The only remaining task is to calculate the partition functions $Q_r(T)$ and $Q^{\ddagger}(T)$. The general expression for the partition function is [42]:

$$Q(T) = \sum_i e^{-E_i/k_B T}, \tag{2.71}$$

where i refers to all molecular states. The total partition function is usually written as a product of the translational, vibrational, rotational, and electronic contributions [42]:

$$Q = Q_{\text{trans}} Q_{\text{rot}} Q_{\text{vibr}} Q_{\text{elec}}. \tag{2.72}$$

The translational partition function of a molecule with total mass m is [42]:

$$Q_{\text{trans}}(T) = V \left(\frac{2\pi m k_B T}{h^2} \right)^{3/2}, \tag{2.73}$$

where V denotes the volume. The rotational contribution can be derived using the rigid rotor approximation, i.e. neglecting the effects of centrifugal distortion. In the case of a linear molecule, the rotational partition function is given by [42]:

$$Q_{\text{rot}}(T) = \frac{2Ik_B T}{\sigma \hbar^2}, \tag{2.74}$$

where I is the moment of inertia and σ denotes the symmetry number. For a non-linear molecule with moments of inertia I_a, I_b, and I_c, the rotational partition function is [27, 42]:

$$Q_{\text{rot}}(T) = \frac{\sqrt{\pi}}{\sigma} \sqrt{\frac{T^3}{\Theta_a \Theta_b \Theta_c}}, \tag{2.75}$$

$$\Theta_i = \frac{\hbar^2}{2I_i k_B}. \tag{2.76}$$

The vibrational partition function can be obtained using the harmonic oscillator approximation, which holds if the degree of vibrational excitation is relatively small. The total vibrational partition function for a molecule with M vibrational modes is then given by [27, 42]:

$$Q_{\text{vibr}}(T) = \prod_{i=1}^{M} \left(1 - e^{-h\nu_i/k_B T} \right)^{-1}, \tag{2.77}$$

where ν_i is the harmonic frequency of mode i. Note that the vibrational partition function for the transition state, $Q^{\ddagger}_{\mathrm{vibr}}(T)$, only contains contributions from the spectator modes. Finally, the expression for $Q_{\mathrm{elec}}(T)$ follows from the consideration that most electronically excited states are inaccessible in the temperature range of interest. The electronic partition function is therefore approximately equal to the degeneracy of the ground state [42]. If, however, several electronic states are thermally accessible, e.g. in the case of spin-orbit coupling, the electronic partition function must be evaluated explicitly.

Chapter 3

Application to OH + CH_4

The reduced dimensionality method described in the previous chapter is suitable for any (pseudo)-triatomic reaction with a collinear reaction path. The present chapter describes how the method is applied to the reaction OH + CH_4 → H_2O + CH_3. The construction of the potential energy surface is discussed in section 3.1 and the numerical details of the dynamics simulations are given in section 3.2.

3.1 Potential energy surface

In this study, the reaction of OH + CH_4 was treated as one of the type (A'A) + B(CD) → (A'A)B + (CD), with (A'A) = OH, B = H', and (CD) = CH_3. The Jacobi coordinates of the product arrangement are R_{CH_3}, the distance between the centers of mass of H_2O and CH_3, and r_{OH}, the distance between the center of mass of OH and H'. The corresponding hyperspherical coordinates are given in Eqs. (2.12) – (2.20), with $m_A = m_O + m_H$ and $m_D = 3m_H$.

The potential energy surface for CH_4OH was calculated on a hyperspherical grid using the Gaussian 03 quantum chemistry package [43]. At each grid point, the geometries were optimized at the MP2 level of theory [44] using the correlation-consistent polarized valence triple-zeta (cc-pVTZ) basis set of Dunning [45]. The reactive O–H' and H'–C bonds remained fixed during the optimization process. After the optimization, the values of ρ and δ were re-evaluated to account for the changes in the centers of mass. The harmonic frequencies for the optimized structures were obtained from a vibrational analysis at the MP2/cc-pVTZ level. The MP2 method is known to perform well in (constrained) geometry optimizations and frequency calculations, but generally tends to overestimate the activation energy [46]. Therefore, the single point energies of the MP2-optimized structures were recalculated at the CCSD(T)/cc-pVTZ level [47] to obtain more accurate results.

The reactive O–H' and H'–C modes were removed from the Hessian using the projection method described in section 2.2. The resulting ZPEs were then added to the CCSD(T)/cc-pVTZ potential to give the effective potential energy surface $V(\rho, \delta)$. At a large number of grid points, however, several spectator modes were found to have imaginary frequencies (i.e negative Hessian eigenvalues). These frequencies ranged from a few wave numbers to $\sim 8000i$ cm^{-1} and were mainly observed at points far off the minimum energy path. Furthermore, the types of modes associated with these frequencies were found to differ from point to point. The problem is most likely

due to the fact that the (partial) geometry optimizations are performed in internal coordinates, while the projection operator is evaluated in Cartesian coordinates. If the internal constraints are not accurately removed from the Hessian, the resulting eigenvalues may be erroneous and imaginary frequencies can occur. Hence, the Hessian and projection operator should be constructed in internal coordinates to evaluate the frequencies. In the present work, however, the contributions from the imaginary frequencies were simply excluded from the effective potential, i.e. only the real parts were used to calculate the ZPEs. The energies of the points with imaginary frequency modes are thus slightly underestimated.

In order to obtain an analytical potential energy surface, the zero-point corrected CCSD(T) energies were fitted to a double Morse potential of the form [27, 29]

$$\begin{aligned} V(\rho,\delta) = &\left(c_1 + c_2\rho^{c_3}e^{-c_4\rho}\right)\Big[\left(1-\exp\Big\{\left(c_5+c_6\rho+c_7\rho^2\right)\delta \right. \\ &\left. + \left(c_8+c_9\rho+c_{10}\rho^2\right) - \log\left(c_{11}+c_{12}\rho+c_{13}\rho^2\right)\Big\}\right)^2 - c_{14}\Big] \\ &+ \left(c_{15}+c_{16}\rho^{c_{17}}e^{-c_{18}\rho}\right)\Big[\left(1-\exp\Big\{-\left(c_{19}+c_{20}\rho+c_{21}\rho^2\right)\delta \right. \\ &\left. + \left(c_{22}+c_{23}\rho+c_{24}\rho^2\right) + \log\left(c_{25}+c_{26}\rho+c_{27}\rho^2\right)\Big\}\right)^2 - c_{28}\Big] + c_{29}. \end{aligned} \tag{3.1}$$

The fitting procedure was performed in MATLAB [48] using a non-linear least squares interative algorithm. First it should be noted that, because the function contains 29 parameters, it is extremely difficult to find a global minimum for the fit. The outcome of the fitting algorithm is therefore strongly dependent on the set of input parameters. Furthermore, the fit must be very accurate in all physically relevant regions, i.e. around the minimum energy path and near the transition state, but is allowed to deviate at higher scattering energies. This readily implies that not all *ab initio* points are equally important to include in the fit. A general approach is to run a series of consecutive fits, each for a different set of points [29]. The initial fit parameters were taken from Ref. [29] for the reaction Cl + CH_4 → HCl + CH_3. These parameters were modified by eye to obtain the correct shape of the potential, and then used as a starting point for the fitting run. The initial fit included all calculated grid points. The output parameters were used as the input parameters for the next fit, which contained fewer *ab initio* points (only those below a certain energy). This procedure was repeated until a small number of low energy points was fitted very accurately. A subset of high energy points was then added to ensure that the potential exhibits the correct behaviour at all accessible energies. In the last fitting run, only the points with zero imaginary frequencies were included. These points, which should be the most accurate, were mainly found at low energies, thus maintaining a good description of all relevant scattering regions. The final fit included a total of 110 *ab initio* points and gave a sum of square residuals of 0.0032 a.u. The corresponding fit parameters are given in Table 3.1. The analytical potential is valid for $6.5 \leq \rho \leq 40$ a.u. and $0 \leq \delta \leq \delta_{max}$.

3.2 Scattering calculations

The scattering calculations for OH + CH_4 were carried out as described in sections 2.3 and 2.4. The coordinate space was divided into 600 sectors of fixed width in ρ ($6.5 \leq \rho \leq 40$ a.u.). Within each sector i, the δ-dependent part of the Hamiltonian

Table 3.1: Optimized fit parameters (in a.u.) for the OH + CH_4 potential.

c_1	0.17930	c_{11}	-69.26464	c_{21}	0.01528
c_2	-8.66368	c_{12}	17.32913	c_{22}	-7.11327
c_3	-1.95123	c_{13}	0.31620	c_{23}	-0.02635
c_4	0.17922	c_{14}	1.51387	c_{24}	0.00019
c_5	24.46518	c_{15}	0.19985	c_{25}	-39.27153
c_6	-0.06029	c_{16}	-3.89436	c_{26}	18.12573
c_7	0.03231	c_{17}	4.54175	c_{27}	-0.24546
c_8	-0.53779	c_{18}	1.76061	c_{28}	1.45754
c_9	0.02501	c_{19}	10.86332	c_{29}	-115.66609
c_{10}	-0.01036	c_{20}	1.12652		

was diagonalized in a discrete variable representation (DVR) basis of 200 particle-in-a-box wave functions [49]. Only the 16 lowest eigenfunctions of $H_\delta^{(i)}$ were included in $\psi_k(\rho, \delta; \rho_i)$, i.e. the wave function expansion of Eq. (2.37) was truncated at $K = 16$. This truncation level was sufficient to allow propagation of all open channels. The R-matrix propagation was repeated for each value of J ($0 \leq J \leq J_{max}$) with J_{max} = 250. Approximate boundary conditions were applied in the last 50 sectors of the propagation. The corresponding state-to-state probabilities were then averaged to obtain the final $P_{ss'}^J(E)$.

The expressions for the reaction cross sections and rate constants are given in section 2.5. The rotational partition function for OH was calculated using the rigid rotor expression of Eq. (2.74) with $I = 5776$ a.u. and $\sigma = 1$. The rotational partition functions for CH_4 and CH_4OH were obtained using Eq. (2.75). For CH_4, the moments of inertia are $I_a = I_b = I_c = 20\,610$ a.u. and $\sigma = 12$. The values for the transition state are $I_a = 27\,059$ a.u., $I_b = 352\,184$ a.u., $I_c = 357\,928$ a.u., and $\sigma = 1$. The harmonic frequencies used to calculate the vibrational partition functions are given in Table 3.2. Note that several transition state frequencies are significantly reduced after projecting out the reactive modes. The imaginary frequency of $1808i$ corresponds to the vibrational motion of H' along the reactive bonds, and thus vanishes completely after projection. The 784 and 927 cm^{-1} modes are primarily CH_4 and H_2O bends coupled to O–H' and H'–C stretching vibrations and the 1293 cm^{-1} mode is a C–H' stretch combined with the umbrella motion of the methyl group. By removing the reactive motions from the Hessian, the 784 and 927 cm^{-1} modes reduce to a single bending mode of 888 cm^{-1}, while the 1293 cm^{-1} mode becomes a pure umbrella motion (1151 cm^{-1}). Another transition state mode that should be mentioned is the 18 cm^{-1} frequency mode, which corresponds to a torsional motion about the C–O axis. Previous studies have shown that this mode must be treated as a hindered internal rotor rather than a harmonic oscillator [17, 18]. The contribution of this mode to the CH_4OH partition function was calculated as follows [20, 50]:

$$Q_{\text{hin}}(T) = \left(1 - e^{-h\nu/k_BT}\right)^{-1} \tanh\left(\frac{\nu}{\sigma_r}\sqrt{\frac{2\pi I_r}{k_BT}}\right), \tag{3.2}$$

with $\sigma_r = 3$ and $I_r = 7690$ a.u. [20]. The remaining modes of the transition state were treated within the harmonic oscillator approximation. The electronic partition

Table 3.2: Harmonic vibrational frequencies calculated at the MP2/cc-pVTZ level of theory. TS (pre) and TS (post) denote the transition state frequencies before and after projection, respectively. All frequencies are in cm^{-1}.

	Frequencies		
OH	3820.6		
CH_4	1349.8	1349.8	1349.8
	1586.3	1586.3	3076.0
	3211.9	3211.9	3211.9
TS (pre)	18.6	314.3	348.4
	784.5	927.2	1206.7
	1293.2	1401.0	1484.8
	1509.8	3116.3	3249.3
	3253.3	3814.4	$1808.8i$
TS (post)	18.6	314.3	350.5
	—	888.6	1206.7
	1151.5	1339.5	1484.9
	1487.8	3103.7	3249.3
	3253.3	3813.7	—
H_2O	1652.1	3855.5	3975.8
CH_3	486.2	1445.4	1445.4
	3177.9	3368.9	3368.9

functions $Q_{\text{elec}}^{\text{CH}_4}(T)$ and $Q_{\text{elec}}^{\ddagger}(T)$ were set to 1 and 2, respectively, assuming a singly degenerate ground state for CH_4 and a doubly degenerate ground state for CH_4OH [20]. The $X\,^2\Pi$ ground state configuration of OH, however, gives rise to four thermally accessible electronic states (neglecting Λ doubling), which occur in two degenerate pairs of $^2\Pi_{3/2}$ and $^2\Pi_{1/2}$ symmetry [20, 24]. The electronic partition function for OH was therefore approximated as:

$$Q_{\text{elec}}^{\text{OH}}(T) = 2 + 2e^{-\Delta E/k_B T}, \tag{3.3}$$

where ΔE is the spin-orbit spitting (139.3 cm^{-1}) between the two components [51].

Finally, to highlight the effect of tunneling, the calculated rate constants were compared to those obtained from classical transition state theory:

$$k_{\text{TST}}(T) = \frac{Q^{\ddagger}(T)}{hQ_{\text{OH}}(T)Q_{\text{CH}_4}(T)} k_B T e^{-\Delta V_a^{\ddagger}/k_B T}, \tag{3.4}$$

where $\Delta V_a^{\ddagger}$ is the vibrationally adiabatic barrier for the reaction. In this expression, the vibrational partition function $Q_{\text{vibr}}^{\ddagger}(T)$ includes all (real) frequencies of the transition state calculated prior to projection.

Chapter 4

Results and discussion

4.1 Electronic structure calculations

The main results of the *ab initio* calculations are summarized in Tables 4.1 and 4.2. Table 4.1 shows the energies of the reactants, products, and transition state at both the MP2/cc-pVTZ and CCSD(T)/cc-pVTZ level of theory. The CCSD(T) method gives a classical barrier height ($\Delta V^{\ddagger}$) of 7.47 kcal mol^{-1} and a classical reaction energy (ΔE) of -10.91 kcal mol^{-1}. Including the ZPE correction yields the vibrationally adiabatic barrier height ($\Delta V_a^{\ddagger}$ = 5.99 kcal mol^{-1}) and the reaction enthalpy at 0 K (ΔH_0 = -12.31 kcal mol^{-1}). The value of ΔE differs by 1.0 kcal mol^{-1} from the best *ab initio* prediction [23] and by 2.6 kcal mol^{-1} from the experimental value (-13.5 kcal mol^{-1}) [52]. The calculated adiabatic barrier height is 1.3 kcal mol^{-1} larger than the $\Delta V_a^{\ddagger}$ value obtained from the most accurate *ab initio* calculations [23].

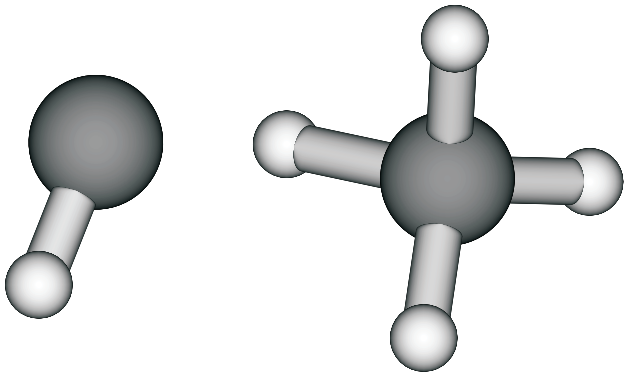

Figure 4.1: Optimized geometry of the CH_4OH transition state.

The optimized structure of the transition state is shown in Fig. 4.1. The corresponding geometry parameters are given in Table 4.2. It can be seen that the transition state is more reactant-like that product-like, thus indicating an early reaction barrier. The C–H' bond at the saddle point is 10% longer than in isolated CH_4, while the O–H' bond is 37% longer compared to that in H_2O. It should be noted, however, that the CH_4OH transition state is not completely collinear. The angle between the reactive bonds, A(OH'C), is 169.37 degrees and the angle between R_{CH_3} and r_{OH} is 173.48 degrees. Since the kinetic energy operator in Eq. (2.29) is defined only for collinear

Table 4.1: Calculated *ab initio* energies of the MP2-optimized geometries using the cc-pVTZ basis set. All energies are in atomic units.

	MP2/cc-pVTZ	CCSD(T)/cc-pVTZ	ZPE
OH	-75.6189	-75.6377	0.0087
CH_4	-40.4117	-40.4381	0.0454
TS	-116.0166	-116.0639	0.0518
H_2O	-76.3187	-76.3322	0.0216
CH_3	-39.7357	-39.7609	0.0303

systems, the reactive scattering Hamiltonian is strictly not valid here. Nevertheless, given that the pseudo-triatomic description of HO–H–CH_3 already represents an approximation to $\hat{H}$, the small deviation from linearity is not expected to have a strong effect on the results of the dynamics simulations.

Table 4.2: MP2-optimized geometries of the reactants, products, and transition state for the reaction OH + CH_4 → H_2O + CH_3. Angles are in degrees and bond lengths in Å. H' represents the abstracted hydrogen atom.

	OH	CH_4	TS	H_2O	CH_3
R(OH)	0.967	—	0.968	0.959	—
R(OH')	—	—	1.316	0.959	—
A(HOH')	—	—	96.979	103.518	—
R(CH)	—	1.085	1.083	—	1.074
R(CH')	—	1.085	1.189	—	—
A(HCH)	—	109.472	112.105	—	120.000
A(HCH')	—	109.472	105.618	—	—
A(OH'C)	—	—	169.370	—	—

Figure 4.2 shows a contour plot of the fitted potential near the transition state. The hyperspherical coordinates at the saddle point are $\rho = 8.38$ a.u. and $\delta = 0.18$ rad ($R_{CH_3} = 2.48$ Å and $r_{OH} = 1.32$ Å). The plot indicates a local minimum at $\rho = 8.82$ a.u. and $\delta = 0.21$ rad, which corresponds to a CH_3–H$\cdots$OH van der Waals complex. This structure has also been found by Basch *et al.* [53] and Yu [26], who reported a CH_3–H$\cdots$OH binding energy of 0.3 and 0.42 kcal mol^{-1}, respectively. In the present work, the well depth of the reactant complex is as large as 2.95 kcal mol^{-1}, but this is an artifact of the fit. The true binding energy is thus expected to be lower. It should also be noted that the fitted potential gives a small (artificial) barrier for the reactant complex at approximately $\rho = 12$ a.u. The effects of both these discrepancies will be discussed in sections 4.2 and 4.4. Another van der Waals complex is located in the product channel ($\rho = 10.9$ a.u. and $\delta = 0.10$ rad), corresponding to the $CH_3\cdots H_2O$ configuration. Basch *et al.* [53] predicted that this complex is unbound at all temperatures, while Masgrau *et al.* [22] found that the well depth is sufficiently large to support bound states. The potential used in this work gives a $CH_3\cdots$H–OH binding energy of 0.56 kcal mol^{-1}, but again this value should be treated with caution.

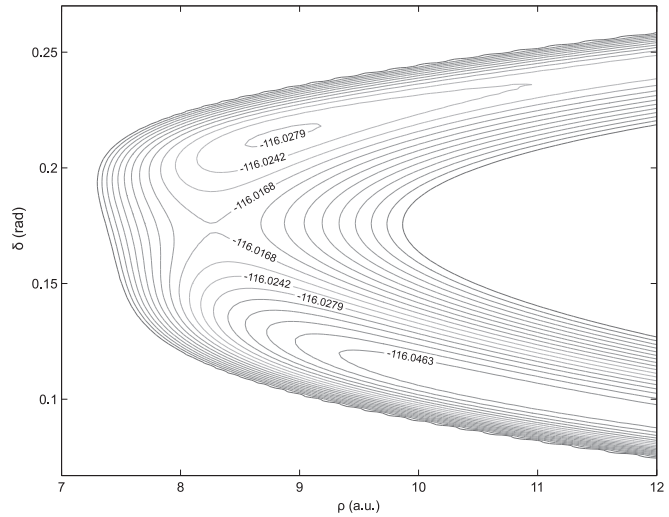

Figure 4.2: Contour plot of $V(\rho, \delta)$ near the transition state. The contour lines range from -116.05 a.u. to -115.98 a.u. In the asymptotic region, $\delta \approx 0$ corresponds to the product arrangement and $\delta \approx \delta_{max}$ to the reactant arrangement.

4.2 Reaction probabilities

The cumulative reaction probability $N^{J=0}(E)$ is shown in Fig. 4.3. The reaction threshold energy is significantly lower than the vibrationally adiabatic barrier height (0.26 eV), indicating a large degree of tunneling. The main state-to-state contributions are plotted in Fig. 4.4. It can be seen that the transition from $s = 0$ to $s' = 0$ dominates at energies below 0.67 eV, while the non-adiabatic $s = 0 \rightarrow s' = 1$ channel becomes important at higher scattering energies. The largest contribution arises from the $s = 1 \rightarrow s' = 2$ channel, which opens at 0.42 eV but only contributes to the CRP at energies above 0.67 eV. This result can be explained by examining the hyperspherical adiabats $\epsilon_s(\rho)$ and $\epsilon_{s'}(\rho)$. Figure 4.5 shows the 10 lowest adiabats as a function of ρ. All of the reactant states exhibit a local maximum at $\rho \approx 12$ a.u., which is due to the van der Waals barrier of the reactant complex. This barrier increases the threshold energy of the $s = 0$ and $s = 1$ states by approximately 0.2 eV.

The hyperspherical adiabats also provide a means for explaining the different magnitudes of the reaction probabilities. It can be seen that the $s = 0$ curve undergoes a weakly avoided crossing with $s' = 1$ at $\rho = 9.2$ a.u., but the avoided crossing with the $s' = 0$ state is much stronger. This crossing is located in the transition state region ($\rho = 8.3$ a.u.), leading to a significant enhancement of the reaction probability. The same holds for the $s = 1 \rightarrow s' = 2$ channel, which proceeds via a strongly avoided crossing at $\rho = 9.2$ a.u. Note that the weakly avoided crossings at $\rho = 20.5$ a.u. ($s = 2 \rightarrow s' = 3$) and $\rho = 18.4$ a.u. ($s = 3 \rightarrow s' = 4$) cannot give rise to large reaction probabilities, since the reactant and product wells are fully separated in this region.

To investigate the influence of the reactant van der Waals well on the CRP, the scattering calculations for $J = 0$ have been repeated using a modified potential that does not possess a CH_3–H$\cdots$OH minimum. The resulting hyperspherical adiabats were found to exhibit much weaker avoided crossings, leading to significantly lower state-to-state reaction probabilities. Based on these findings, it can be concluded that

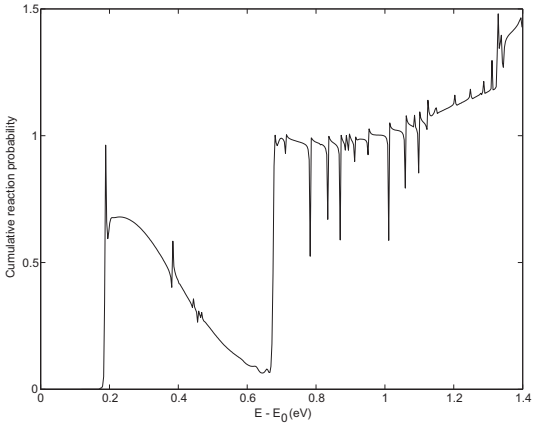

Figure 4.3: Cumulative reaction probability for $J = 0$ as a function of the initial translation energy. E_0 is the ground state energy of the reactants.

the existence of a reactant van der Waals complex near the transition state greatly enhances the CRP. This result is physically intuitive, since a metastable minimum in the entrance channel provides more time for the reactants to break through the barrier. Nevertheless, it should be noted that the optimized potential used in this work overestimates the $CH_4 \cdots OH$ well depth by ~ 2.5 kcal mol^{-1} [26, 53], implying that the calculated reaction probabilities are also somewhat overestimated.

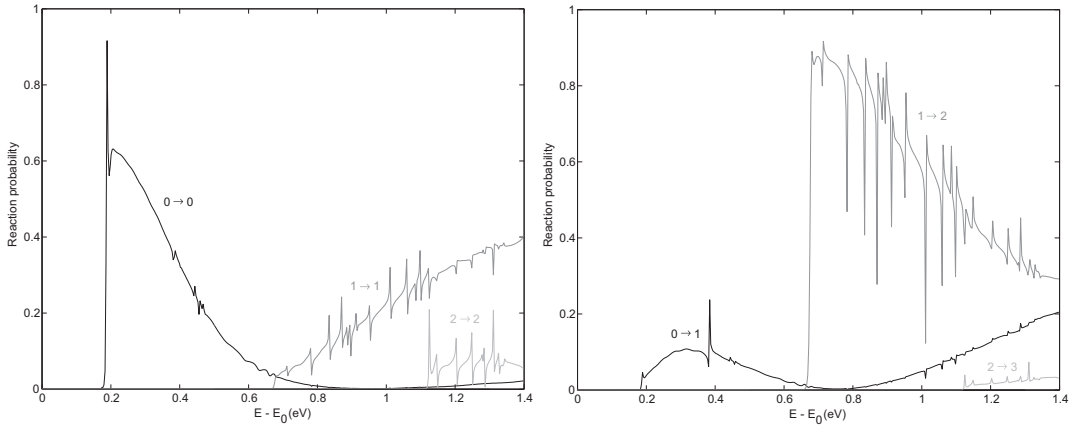

Figure 4.4: State-to-state reaction probabilities for $OH + CH_4(s) \rightarrow H_2O(s') + CH_3$ as a function of the initial translation energy; (a) vibrationally adiabatic, (b) vibrationally non-adiabatic.

4.3 Integral and differential cross sections

The initial state-selected integral reaction cross sections $\sigma_s(E)$ are shown in Fig. 4.6. The $s = 0$ curve dominates at low scattering energies, which is mainly due to the adiabatic $s = 0 \rightarrow s' = 0$ transition. It can also be seen that excitation of the C–H' stretch ($s = 1$) leads to a significant enhancement of the total reaction cross section. These findings are consistent with the reduced dimensionality quantum scattering

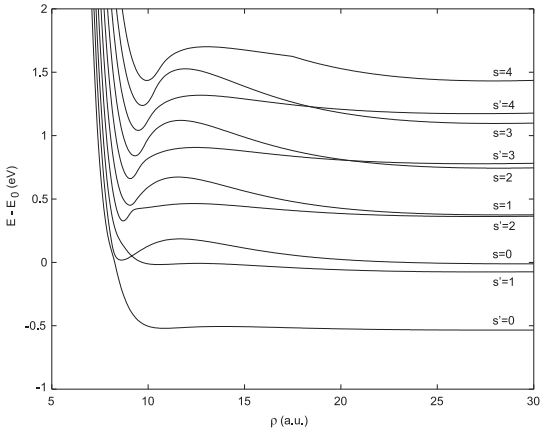

Figure 4.5: Hyperspherical adiabats for OH + $CH_4(s) \rightarrow H_2O(s') + CH_3$. The energy is defined relative to the ground state of the reactants.

calculations of Nyman and Clary [24] and Yu [26]. It should be noted, however, that the shape of the $\sigma_1(E)$ curve is somewhat different than that reported by Nyman and Clary. This discrepancy is likely to be caused by the difference in the potential energy surfaces used.

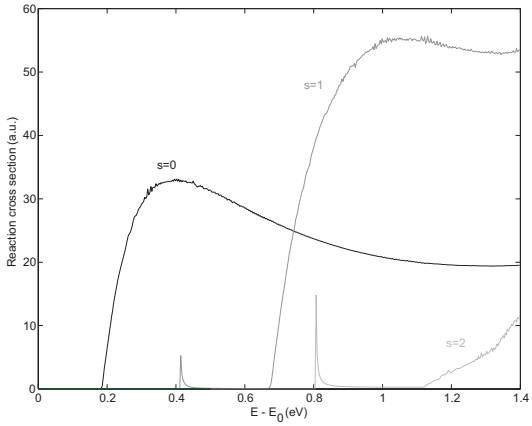

Figure 4.6: Initial state-selected reaction cross sections as a function of the initial translational energy.

Figure 4.7 shows the state-to-state differential cross sections as a function of the scattering angle. As already mentioned in section 2.5, the values of $\sigma_{ss'}(\theta)$ may be slightly inaccurate due to the use of approximate boundary conditions. Nevertheless, previous work on Cl + $CH_4 \rightarrow$ HCl + CH_3 has shown that this approximation does not significantly alter the qualitative result [29]. Figure 4.7(a) compares the state-to-state differential cross sections for $s = 0 \rightarrow s' = 0$ and $s = 1 \rightarrow s' = 2$ at an energy of 0.75 eV. The scattering energy is defined relative to the ground state of the reactants. It can be seen that the $s' = 0$ product is predominantly sideways scattered, while the $s' = 2$ product shows a broad backward scattering peak. The energy dependence of $\sigma_{00}(\theta)$ is plotted in Fig. 4.7(b). There is a propensity for backward scattering at low translational energies ($E = 0.20$ eV) and an increasingly strong tendency towards

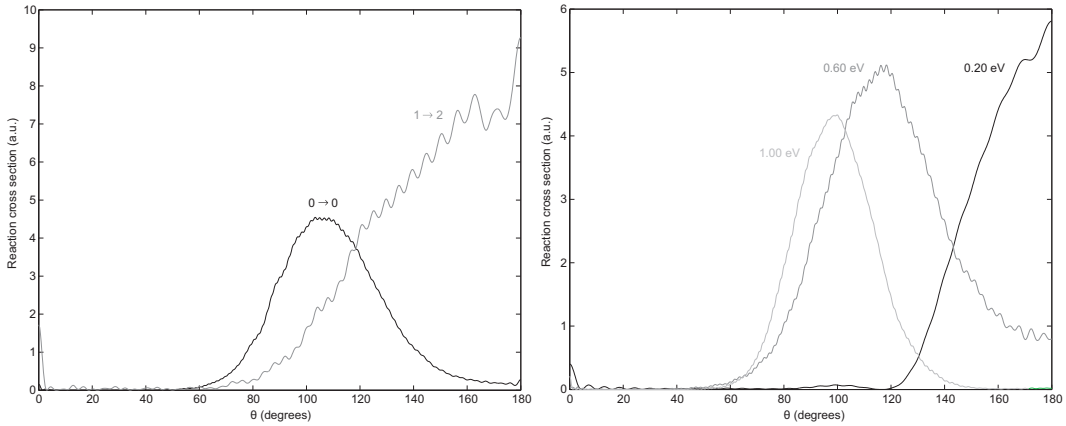

Figure 4.7: State-to-state differential cross sections for (a) $s = 0 \rightarrow s' = 0$ and $s = 1 \rightarrow s' = 2$ at 0.75 eV and (b) $s = 0 \rightarrow s' = 0$ at 0.20, 0.60, and 1.00 eV.

sideways scattering as E becomes larger. These results are in good agreement with the work of Nyman *et al.* [25].

4.4 State-to-state and thermal rate constants

The calculated rate constants are presented in Table 4.3 and Fig. 4.8. It can be seen from Table 4.3 that the adiabatic $s = 0 \rightarrow s' = 0$ transition gives the largest contribution to $k(T)$, which is due to the high reaction probability for this channel. Figure 4.8 compares the calculated quantum rates to the experimental data. The results are in very good agreement over the entire temperature range of interest, suggesting that the approximation of treating only two degrees of freedom in the scattering is reasonable. The calculated quantum rates also compare favorably with the reduced dimensionality quantum dynamics study of Yu [26], in which five degrees of freedom were treated explicitly. Nevertheless, it must be noted that the curvature of the Arrhenius plot is not completely reproduced in the present calculations. The deviation from experiment is either due to approximations in the dynamics simulations or the use of an imperfect potential energy surface.

The sensitivity to the potential becomes apparent when examining the influence of the $CH_4 \cdots OH$ van der Waals well. The rate constants obtained from the modified potential energy surface, i.e. the surface without a $CH_4 \cdots OH$ minimum, were found to be several orders of magnitude lower across the entire range of T. The reactant complex thus has a very strong influence on the reaction rate. It must be noted, however, that the optimized potential overestimates the van der Waals well depth by ~ 2.5 kcal mol^{-1}, which should result in an overestimation of the rate constant. Since this behaviour is not observed at all temperatures, there must be other sources of error involved. As already suggested by Masgrau *et al.* [22], the MP2/cc-pVTZ and CCSD(T)/cc-pVTZ levels of theory may not be fully adequate to accurately describe the CH_4OH potential energy surface. An imperfect fit to the *ab initio* points could further increase the error in $V(\rho, \delta)$. In view of the latter, the use of a numerical interpolation algorithm could possibly lead to improved results.

Finally, to highlight the need for a quantum mechanical treatment, the rates are

Table 4.3: State-to-state and thermal rate constants (in cm^3 $molecule^{-1}$ s^{-1}) for the reaction OH + CH_4 → H_2O + CH_3. Numbers in parentheses denote powers of 10.

T (K)	k_{00}	k_{01}	k_{11}	k_{12}	k_{22}	k_{total}
200	2.56(-16)	1.71(-17)	1.05(-25)	3.85(-28)	3.25(-34)	2.73(-16)
250	1.85(-15)	1.34(-16)	8.97(-24)	3.69(-25)	2.50(-30)	1.99(-15)
298	6.74(-15)	5.24(-16)	1.61(-22)	4.94(-23)	8.11(-28)	7.27(-15)
300	7.05(-15)	5.49(-16)	1.78(-22)	5.86(-23)	9.91(-28)	7.60(-15)
350	1.87(-14)	1.55(-15)	1.62(-21)	2.32(-21)	7.27(-26)	2.02(-14)
400	3.95(-14)	3.49(-15)	9.64(-21)	3.74(-20)	1.86(-24)	4.30(-14)
450	7.20(-14)	6.69(-15)	4.65(-20)	3.32(-19)	2.38(-23)	7.87(-14)
500	1.18(-13)	1.15(-14)	1.95(-19)	1.94(-18)	1.88(-22)	1.30(-13)
600	2.57(-13)	2.72(-14)	2.27(-18)	2.84(-17)	4.52(-21)	2.84(-13)
700	4.64(-13)	5.26(-14)	1.59(-17)	2.01(-16)	4.95(-20)	5.17(-13)
800	7.43(-13)	8.91(-14)	7.43(-17)	9.01(-16)	3.35(-19)	8.34(-13)
1000	1.51(-12)	1.98(-13)	7.30(-16)	7.80(-15)	6.17(-18)	1.72(-12)
1300	3.13(-12)	4.51(-13)	7.06(-15)	6.24(-14)	1.19(-16)	3.65(-12)
1600	5.15(-12)	7.95(-13)	3.23(-14)	2.43(-13)	8.61(-16)	6.24(-12)
2000	8.21(-12)	1.36(-12)	1.30(-13)	8.25(-13)	5.09(-15)	1.06(-11)

compared to those obtained from classical transition state theory (Fig. 4.8). The TST curve strongly underestimates the rate constant at low temperatures, indicating the importance of tunneling. Furthermore, the neglect of recrossing leads to an overestimation of $k(T)$ at temperatures above ~ 1250 K. A rigorous treatment of both tunneling and recrossing effects is thus crucial for accurately predicting the rate constant.

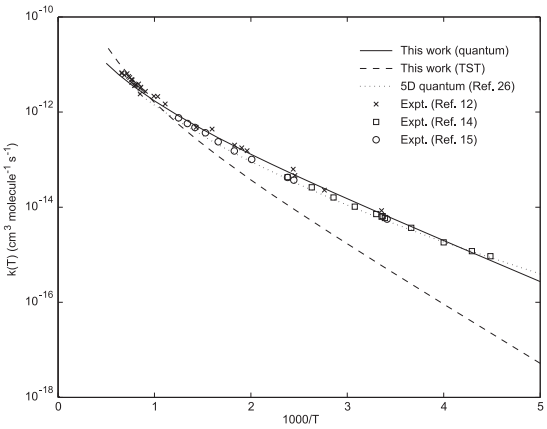

Figure 4.8: Thermal rate constants for OH + CH_4 → H_2O + CH_3.

Chapter 5

Conclusions

A two-dimensional quantum scattering method has been described for studying the dynamics and kinetics of collinear (polyatomic) reactions. The method treats explicitly the bonds being broken and formed, while the remaining spectator bonds are accounted for by means of an effective potential. State-to-state reaction probabilities are obtained by propagating the R-matrix in hyperspherical coordinates and enforcing approximate boundary conditions at the end of the propagation. The main advantage of this reduced dimensionality method lies in the fact that only a small number of *ab initio* calculations is needed to develop the potential energy surface, offering a computationally efficient route to kinetic and dynamic properties.

The method has been used to calculate state-selected reaction cross sections and rate constants for the reaction OH + CH_4 → H_2O + CH_3. The effective potential energy surface was obtained by fitting a double Morse function of 29 parameters to a set of high level *ab initio* points. The *ab initio* calculations were performed at the CCSD(T)/cc-pVTZ level of theory using MP2/cc-pVTZ optimized geometries. The zero-point energies of the spectator modes were included prior to fitting to account for the quantum nature of the neglected degrees of freedom.

The results indicate that the ground state reaction of OH + CH_4 yields predominantly ground state products, with a minor fraction of vibrationally excited H_2O. Furthermore, it has been found that excitation of the C–H stretch leads to a significant enhancement of the total reaction cross section. The calculated differential cross sections show that the H_2O product is mainly scattered in the backward hemisphere, with a strong propensity for sideways scattering at high translational energies. Finally, the rate constants reveal that quantum effects play an important role in the reaction. The calculated rates compare very favorably with the experimental results, although the curvature of the Arrhenius plot is not completely reproduced. This is most likely due to inaccuracies in the potential energy surface used. Nevertheless, the comparison with experiment suggests that the approximation of treating only two degrees of freedom explicitly is reasonable.

Bibliography

[1] J. M. Bowman and G. C. Schatz, Annu. Rev. Phys. Chem. **46**, 169 (1995).

[2] S. C. Althorpe and S. C. Clary, Annu. Rev. Phys. Chem. **54**, 493 (2003).

[3] D. G. Truhlar, B. C. Garrett, and S. J. Klippenstein, J. Phys. Chem. **100**, 12771 (1996).

[4] J. M. Bowman and A. F. Wagner, in *The Theory of Chemical Reaction Dynamics*, edited by D. C. Clary (Reidel, Dordrecht, 1986), p. 47.

[5] N. R. Greiner, J. Chem. Phys. **53**, 1070 (1970).

[6] D. D. Davis, S. Fischer, and R. Schiff, J. Chem. Phys. **61**, 2213 (1974).

[7] R. Zellner and W. Steinert, Int. J. Chem. Kinet. **8**, 397 (1976).

[8] F. P. Tully and A. R. Ravishankara, J. Phys. Chem. **84**, 3126 (1980).

[9] K.-M. Jeong and F. Kaufman, J. Phys. Chem. **86**, 1808 (1982).

[10] D. L. Baulch, R. J. B. Craven, M. Din, D. D. Drysdale, S. Grant, D. J. Richardson, A. Walker, and G. Watling, J. Chem. Soc. Faraday Trans. **79**, 689 (1983).

[11] C. D. Jonah, W. A. Mulac, and P. Zeglinski, J. Phys. Chem. **88**, 4100 (1984).

[12] S. Madronich and W. Felder, 20th Int. Symp. Combustion (The Combustion Institute, Pittburgh, PA, 1984), p. 703.

[13] J. F. Bott and N. Cohen, Int. J. Chem. Kinet. **21**, 485 (1989).

[14] G. L. Vaghjiani and A. R. Ravishankara, Nature **350**, 406 (1991).

[15] J. R. Dunlop and F. P. Tully, J. Phys. Chem. **97**, 11148 (1993).

[16] T. Gierczak, R. K. Talukdar, S. C. Herndon, G. L. Vaghjiani, and A. R. Ravishankara, J. Phys. Chem. A **101**, 3125 (1997).

[17] T. N. Truong and D. G. Truhlar, J. Chem. Phys. **93**, 1761 (1990).

[18] C. Gonzalez, J. J. W. McDouall, and H. B. Schlegel, J. Phys. Chem. **94**, 7467 (1990).

[19] K. D. Dobbs and D. A. Dixon, J. Chem. Phys. **98**, 8852 (1993).

[20] V. S. Melissas and D. G. Truhlar, J. Chem. Phys. **99**, 1013 (1993).

[21] J. Espinosa-Garcia and J. C. Corchado, J. Chem. Phys. **112**, 5731 (2000).

[22] L. Masgrau, A. Gonzalez-Lafont, and J. M. Lluch, J. Chem. Phys. **114**, 2154 (2001).

[23] L. Masgrau, A. Gonzalez-Lafont, and J. M. Lluch, J. Chem. Phys. **115**, 4515 (2001).

[24] G. Nyman and D. C. Clary, J. Chem. Phys. **101**, 5756 (1994).

[25] G. Nyman, D. C. Clary, and R. D. Levine, Chem. Phys. **191**, 223 (1995).

[26] H.-G. Yu, J. Chem. Phys. **114**, 2967 (2001).

[27] B. Kerkeni and D. C. Clary, J. Chem. Phys. **120**, 2308 (2004).

[28] B. Kerkeni and D. C. Clary, Phys. Chem. Chem. Phys. **8**, 917 (2005).

[29] S. T. Banks and D. C. Clary, Phys. Chem. Chem. Phys. **9**, 933 (2007).

[30] D. E. Manolopoulos, in *The Encyclopedia of Computational Chemistry*, edited by P. v. R. Schleyer (Wiley, Chichester, 1998), p. 2699.

[31] R. B. Walker and E. F. Hayes, in *The Theory of Chemical Reaction Dynamics*, edited by D. C. Clary (Reidel, Dordrecht, 1986), p. 105.

[32] J. M. Bowman, G.-Z. Ju, and K. T. Lee, J. Phys. Chem. **86**, 2232 (1982).

[33] Q. Sun and J. M. Bowman, Int. J. Quantum Chem., Symp. **23**, 115 (1989).

[34] Q. Sun and J. M. Bowman, J. Chem. Phys. **92**, 5201 (1990).

[35] F. Jensen, *Introduction to Computational Chemistry* (Wiley, Chichester, 1999).

[36] J. W. Ochterski, *Vibrational Analysis in Gaussian*, http://www.gaussian.com.

[37] D. Lu and D. G. Truhlar, J. Chem. Phys. **99**, 2723 (1993).

[38] E. B. Stechel, R. B. Walker, and J. C. Light, J. Chem. Phys. **69**, 3518 (1978).

[39] D. C. Clary, J. Chem. Phys. **95**, 7298 (1991).

[40] T. Xie, J. M. Bowman, K. A. Peterson, and B. Ramachandran, J. Chem. Phys. **119**, 9601 (2003).

[41] J. M. Bowman, J. Phys. Chem. **95**, 4960 (1991).

[42] P. W. Atkins, *Physical Chemistry* (Oxford University Press, Oxford, 1986).

[43] M. J. Frisch, G. W. Trucks, H. B. Schlegel, G. E. Scuseria, M. A. Robb, J. R. Cheeseman, J. A. Montgomery, Jr., T. Vreven, K. N. Kudin, J. C. Burant *et al.*, GAUSSIAN 03, Revision C.02, Gaussian, Inc., Wallingford, CT (2004).

[44] C. Møller and M. S. Plesset, Phys. Rev. **46**, 618 (1934).

[45] T. H. Dunning, Jr., J. Chem. Phys. **90**, 1007 (1989).

[46] B. Kerkeni and D. C. Clary, Phys. Chem. Chem. Phys. **8**, 917 (2006).

[47] K. Raghavachari, G. W. Trucks, J. A. Pople, and M. Head-Gordon, Chem. Phys. Lett. **157**, 479 (1989).

[48] MATLAB is a registered trademark of The MathWorks, Inc. (Natick, MA).

[49] J. T. Muckerman, Chem. Phys. Lett. **173**, 200 (1990).

[50] D. G. Truhlar, J. Comput. Chem. **12**, 266 (1991).

[51] M. P. J. van der Loo and G. C. Groenenboom, J. Chem. Phys. **126**, 114314 (2007).

[52] R. Atkinson, J. Phys. Chem. Ref. Data Monograph **1**, 18 (1989).

[53] H. Basch and S. Hoz, J. Phys. Chem. A **101**, 4416 (1997).